Investigation of Zinc Oxide Nanowires for Impedance Based Structural Health Monitoring

Sean A. Offenberger

Thesis submitted to the faculty of the Virginia Polytechnic Institute and State University in partial fulfillment of the requirements for the degree of

Master of Science
in
Aerospace Engineering

Michael Philen, Chair
Mayuresh Patil
Gary D. Seidel

February 16 2018
Blacksburg, Virginia

Keywords: Smart Materials, Piezoelectrics, Zinc Oxide Nanowires, Impedance-Based Structural Health Monitoring

Investigation of Zinc Oxide Nanowires for Impedance Based Structural Health Monitoring

Sean Offenberger

Abstract

The goal of this work is to investigate the piezoelectricity of composite laminates embedded with layers of zinc oxide (ZnO) nanowires. ZnO nanowire embedded composites have the potential to sense and actuate giving the potential for these smart composites to serve the function of being load bearing structures and monitoring the integrity of the structure. This work examines the piezoelectric characteristics of composite beams by investigating their electromechanical coupling in the form of vibration under the presence of electrical excitation. With the help of a mathematical model, piezoelectric constants are estimated for these samples. A layer of ZnO nanowires were grown on plane woven fiberglass fabric that was incorporated into a carbon fiber epoxy composite. The beam deflection velocity was measured as a varying voltage was applied to the composite. Using Hamilton's Principle and Galerkin's method of weighted residuals, a mathematical model was derived to estimate piezoelectric constants for the composites from the experimental data. Piezoelectric properties were determined using vibrational testing and a mathematical model. Piezoelectric constants h_{31}, g_{31}, and d_{31} were estimated to be 9.138 E7 V/m, 6.092 E-4 Vm/N, and 2.46 E-14 respectively. To demonstrate the electromechanical coupling, ZnO nanowire composites were bonded to Al beams that were progressively damaged to determine if a change in electrical impedance could be observed to correspond to the change in structural impedance of the host beam. Changes in impedance were detected by a change in root mean squared deviation damage metric M. A significant correlation was shown between increasing damage in the host beam and an increase in damage metric M.

Investigation of Zinc Oxide Nanowires for Impedance Based Structural Health Monitoring

Sean Offenberger

General Audience Abstract

A major problem facing both commercial and military aircraft fleets is aircraft grounded time due to inspection. Inspection times tend to be lengthy since visual inspection cannot detect all types of incurred damage an aircraft may face. In the case of composite aircraft structures, a special type of damage known as delamination (when layers of the composite structure become un-bonded) can occur. Since delamination is not always visible from the surface, and composite structures cannot be taken apart since they are made in one piece; additional damage detection methods are necessary. Impedance-based structural health monitoring (IBSHM) is one technique of nondestructive evaluation (NDE) that examines changes in vibrational response of the structure in order to detect damage. A novel approach to IBSHM is incorporating zinc oxide, a type of piezoelectric material, inside the composites due to its ability to deform in the presence of an electric field or generate a voltage when stressed. The goal of this research is to determine piezoelectric properties of composites with ZnO nanowires grown on inner layers of the laminates. Piezoelectric properties were determined using vibrational testing and a mathematical model. To demonstrate the electromechanical coupling, ZnO nanowire composites were bonded to Al beams that were progressively damaged to determine if a change in electrical impedance could be observed to correspond to the change in structural impedance of the host beam. Changes in impedance were detected by a change in root mean squared deviation damage metric M. A significant correlation was shown between increasing damage in the host beam and an increase in damage metric M.

Acknowledgements

I would like to thank my advisor and committee chair Michael Philen for his continued guidance and assistance, both financial and intellectual, throughout my graduate studies.

I would also like to thank my lab mates in the Aerospace Structures and Materials Laboratory, Howard Chung, Julian Brown, Lori Groo, and Brady Doepke for their comradery and help while working in the lab.

I would like to thank my parents and grandparents for their continued belief and support throughout my time at Virginia Tech. Also, for instilling in me a love for math and science and giving me the tools to be successful academically. Without them I could have never done this.

Finally I would like to thank my girlfriend Laura Leigh for challenging me to be my best self, never settle for good enough, and believing in me even when I didn't believe in myself.

Table of Contents

Table of Figures

List of Tables

Chapter 1 Introduction

1.1 Motivation

In 2003, it was estimated that the cost of keeping an aircraft grounded due to unscheduled maintenance is $23,000/hr [1]. In 2007 alone, the total global market for Aviation Maintenance, Repair, and Overhaul (AMRO) was valued at $117 billion, $31 billion of which was contributed to the United State Department of Defense for maintenance of their 13,521 aircraft fleet [2, 3]. The average age of US military aircraft is 23 years, with an extra 25 years of expected service for more than half of them[4]. As the fleet ages, the amount of AMRO is only set to increase. However, with the use of innovative structural health monitoring (SHM) systems, it is estimated that that inspection time could be reduced by 40 percent or more [5].

Impedance-Based SHM (IBSHM) is a popular technique for investigating the health of structures since it does not require disassembly or local inspection from special equipment. IBSHM operates by attaching actuators and sensors to a structure, vibrating it, and reading its mechanical impedance. It is then converted into electrical impedance where it is interpreted by a computer. The actuators and sensors are made of piezoelectric materials, which have electrical/mechanical coupling. This means that in the presence of mechanical stress, an electrical polarization occurs, or conversely a strain is produced from the application of an electrical field, known as the direct and indirect piezoelectric effect respectively.

In order to measure damage with IBSHM, impedances are taken for the structure before any damage is incurred. That way, any shift in the impedance readings can be used to indicate the type and magnitude of damage present in the structure. This method presents several challenges for practical applications. These piezoelectric actuators/sensors can only detect damage within their immediate vicinity. In order to detect damage across the whole structure, the piezoelectrics must be placed across its entirety, instead of at just a few

strategic locations. This results in an undesired increase in structural weight, not just from the actuators, but also from the associated wires and hardware needed to operate them [6]. This also necessitates that all the piezoelectrics maintain proper bonding to the structure throughout its lifetime of use. Since these actuators and sensors must be placed at interior locations, replacing de-bonded piezoelectrics becomes complicated and costly. Finally, the same problem is incurred if any of the sensors fail and need replacing. In order to combat these issues, several researchers have proposed integrating the piezoelectrics into the structure, for example in between plies of a composite [5, 7-11]. This would create a continuous piezoelectric system embedded within the structure which would be able to pinpoint the location and type of damage, as well as reduce the amount of wiring needed to complete the system in addition to removing the concern over sensor debonding. However, at the points where the piezoelectric actuators/sensors were introduced into the composite, there is an increase in the potential for delamination due to poor bonding between the piezoelectrics and matrix. To combat this, researchers have proposed integrating nanoparticles/structures into the composite to form a piezoelectric layer that fits seamlessly into the laminate and would not increase the potential for delamination [10, 12, 13].

1.2 History and Current Technology

1.2.1 History of Piezoelectricity

Jacques and Pierre Curie discovered the direct piezoelectric effect in 1880, when they observed that compression of asymmetric crystals about their hemithedral axis generated electrical polarization [14-17]. They found the effect in boracite, calamine, cane sugar, quartz, Rochelle salt, sodium chlorate, tartaric acid, topaz, tourmaline, and zinc blende [14, 16]. In late 1881 (working primarily with tourmaline), they confirmed the inverse effect, and the following year the Curies confirmed its magnitude [14-16]. The inverse effect had been predicted earlier that year by Gabriel Lippmann [18].

Instead of publishing their results, the Curies made an announcement to the French Academy of Sciences in 1881 listing the following discoveries:

1. The two ends of tourmaline release equal quantities of electricity of opposite signs.
2. The quantity released by a certain increase of pressure is the opposite sign and equal to that produced by an equal decrease in pressure.
3. This quantity is proportional to the variation of pressure.
4. It is independent of the tourmaline's length.
5. For some variation of pressure per unit of surface area, it is proportional to the area [18].

Of particular importance is the conclusion derived from the last two statements, that the amount of electricity produced by an induced pressure is independent of the size of the tourmaline [14].

In 1894 Woldemar Voigt created a model connecting piezoelectricity to crystal symmetry [14-16]. With this model, he was able to predict that there are 32 classes of crystals that are capable of generating piezoelectric effect, as well as predicting how many of the 18 piezoelectric coefficients each class would require [16].

Piezoelectrics found their first practical application around World War I, when Paul Langevin used quartz crystals to create a sonar device for locating submarines and determining their distance from the ocean floor [16]. In 1945, the ceramic Barium titanate ($BaTiO_3$) was discovered by both Von Hippel from MIT and Vul and Goldman of the USSR [15, 16]. This created an interest in researching ceramics as a piezoelectric material leading to the discovery of the lead zirconate titanate ($Pb(Zr\text{-}Ti)O_3$ or PZT) [15]. In 1969 Heiji Kawai, published a paper on a thin polymer film, polyvinylidene fluoride (PVDF), which produced a piezoelectricity much larger than quartz [15, 16].

1.2.2 Zinc Oxide

Zinc oxide (ZnO) has been a popular piezoelectric material since the 1960's due to wide range of applications including catalysts, sensors, and transducers [19]. ZnO is a wurtzite type structure, characterized by its hexagonal shape with polar surfaces and no central axis of symmetry, which displays properties of both piezoelectric and semiconducting materials [19-22]. As Voigt predicted in his model, this asymmetry of the crystal structure is what gives ZnO its piezoelectric properties [14-16]. The polar surface of ZnO is made up of tetrahedrally arranged Zn^{2+} and O^{2-} ion planes that alternate along the c-axis [20]. This structure is shown in Figure 1.

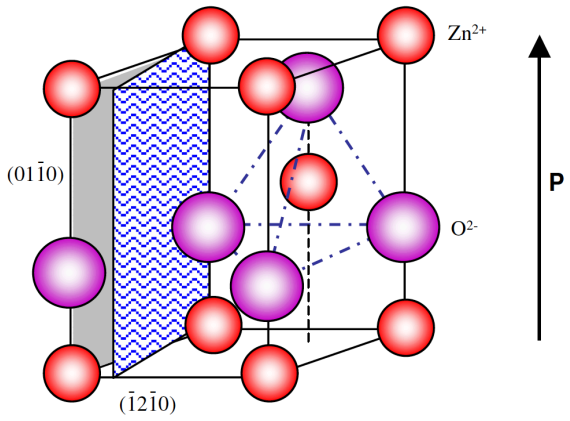

Figure 1. Wurtzite structure of ZnO[19]

This surface geometry allows for ZnO to be arranged in a wide arrange of nanostructures including: nanorings, nanosprings, nanowires/rods, nanobelts, nanopropellers, nanotubes, nanocombs, and nanocages [19-21].

Nanowires (or nanorods) are of particular interest due to their ability to grow on substrate layers within composite structures. Nanowires are formed using the vapor-liquid-solid (VLS) process, in which a liquid droplet made up of a metal and the nanowire material (Au and ZnO in this case) is placed on the substrate [19, 20, 23, 24]. The liquid then absorbs vapor reactants until it becomes supersaturated, causing the growth of the nanowire [19]. The growth continues until the catalyst transitions from liquid to solid, forming a solid nanoparticle at the nanowire's tip [19]. The growth direction and diameter of the nanowire are determined by the catalyst droplet, resulting in the solid catalyst tip having the same diameter as the rest of the nanowire. Figure 2 shows an SEM image of the ZnO/Au nanorods.

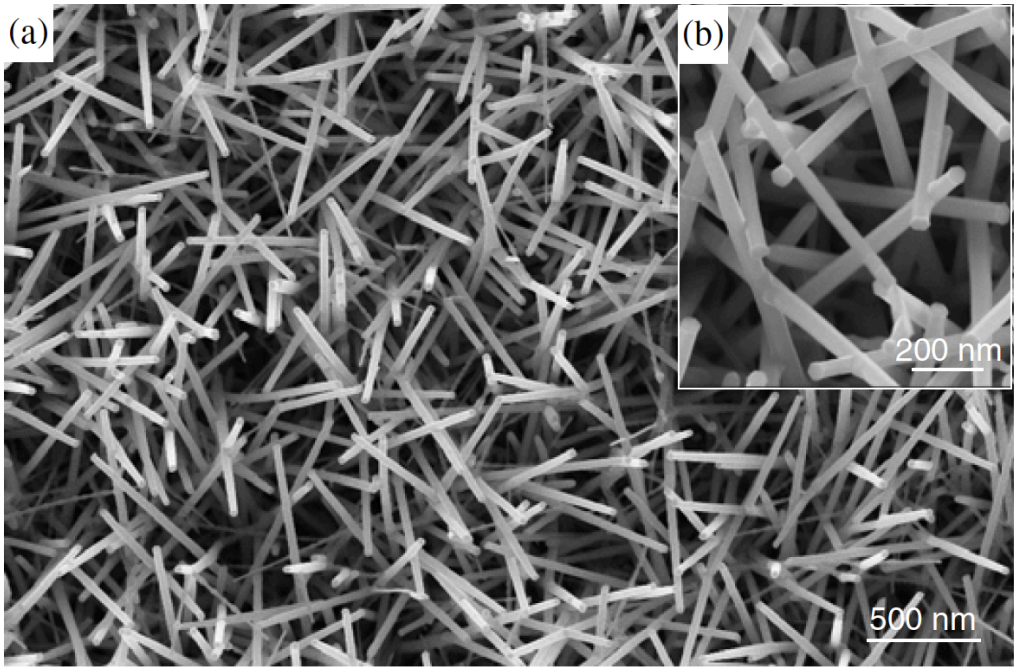

Figure 2. (a) ZnO nanorods formed with Au catalyst. (b) Close up image of nanorods where solid Au tip can be more easily seen.[19]

When the nanowires are incorporated into composites, they are able to convert the mechanical energy of their vibrations into an electrical charge. When the nanowires rub against each other as they deflect, it causes a separation of the charge centers of the ions along the wires [24]. This creates a potential along the wires, which is then balanced by the flow of electrons along the circuit created by the ZnO [24].

In addition to its piezoelectric properties, ZnO also displays strong semiconducting behavior. ZnO is a wide band-gap material displaying a gap of 3.37 eV[19]. Wide band-gap materials are characterized by a band gap of greater than 2 eV. Band gaps are the energy required for bonded valence electrons to become conduction electrons, which can carry charges and create a circuit [25]. Wide band-gap semiconductors are an emerging technology that offers the potential for smaller, faster, and more efficient electronics, which are vital for the smart materials [26].

1.2.3 Structural Health Monitoring

Before the availability of modern structural health monitoring techniques, aircraft were rated for a certain number of flight hours and retired once that number had been reached [7]. In between flights, damage detection relied mainly on visual inspection.

However as aircraft components changed from simple aluminum walled structures to more complicated ones (such as composites), more rigorous detection methods were required [27]. Composites are incredibly susceptible to delamination, a failure mode in which components of the composite de-bonded from the rest of the structure [28]. Composite delamination is not always visibly apparent, so either the structure must be taken apart to inspect for damage, or a method of nondestructive evaluation (NDE) must be applied to inspect the part. Since composite components are frequently constructed as a single continuous part, small sections cannot be removed for local inspection, as is the case with traditional aluminum walled structures. Therefore, NDE is the only way to inspect the part without causing irrevocable damage.

Examples of NDE Methods include: acoustic emissions, magnetic imaging, optical methods, radiology, and ultrasound [7, 29]. Many of these methods are time consuming and unwieldy, especially when applied to structures that are large or not easily accessible, such as windmills, off-shore drilling rigs, and space structures [27, 28]. However, if structural health monitoring technology is incorporated into the structure itself, the resulting "smart material" would be able to eliminate this problem [6, 7, 28].

These integrated SHM systems could utilize the impedance method, which relies on the mechanical/electrical coupling of piezoelectric materials, and falls into two categories based upon the scope of its vibration and detection abilities: local and global [30].

Park, Inman, and Sun have utilized local impedance based structural health monitoring to detect damage by vibrating a piezoelectric patch that is bonded to a structure and reading the mechanical impedance that results from the vibrations [31, 32]. This reading is then compared to an initial reading of the undamaged structure to determine the presence and severity of damage [33]. While this system is easy to implement, it only looks at the area in the vicinity of the patch. This means the patch, or a series of patches, must be strategically placed on the structure and individually tested to search for damage in each patch's vicinity.

Global SHM on the other hand, incorporates a network of sensors across a structure, which gives a complete picture of the structure's health. There are several different approaches to this method; including embedded fiber optic cables that observe changes in

the wavelength of the light transmitted through the cable to detect strains; microwave sensors that can be used remotely and in high temperature situations; and acoustic actuators and sensors that observe differences in the vibration of the structure [7, 10, 30, 34-37]. Any change in vibration indicates damage such as dents, delamination, or cracks [7, 10, 30, 34-37]. With each method, the data collected from all of the sensors must be consolidated in a process known as data fusion [30]. Different methods from data fusion range from comparing data between sensors to creating artificial neural networks (ANN) amongst all of the sensors as demonstrated by Abdeljaber, de Oliveira, Inman, Lopez, and Park [27, 38, 39]. These ANN are a type of statistical model which rely on supervised learning, which compares data taken from the damaged and undamaged structure [27, 30]. In general, however, ANNs are a type of artificial intelligence (AI) that is gaining popularity across several fields of technology and engineering including analytical chemistry, anatomy, environmental engineering, finance, manufacturing, medicine, and structural engineering [38, 40-43].

1.3 Problem Statement and Objectives

Zinc oxide nanowires were incorporated into carbon fiber/epoxy composites to investigate their potential as a piezoelectric material for IBSHM.

The objectives of this research are as follows:

1. Determine effectiveness of the ZnO integrated composites for piezoelectric applications.
2. Determine the effective piezoelectric properties of the ZnO composites.
3. Demonstrate their ability to detect damage in a structure in which the ZnO composites are incorporated.

In order to determine the effectiveness of ZnO integrated composites, they were tested to determine their electromechanical properties, found by comparing experimental results to a mathematical model developed for the composites. They were then bonded to beams, which were tested to determine their impedance over a range of frequencies. The beams were then progressively damaged in order to see if a change in impedance could be observed.

1.4 Thesis Organization

The following will serve as the organizational structure of the thesis:

Chapter 1 Introduction and literature review is provided.

Chapter 2 A mathematical model will be derived for the electromechanical behavior of the ZnO incorporated composites.

Chapter 3 An explanation will be presented of the experiments performed, as well as a description of the composite fabrication.

Chapter 4 Analysis of the experimental data and analysis model will be provided.

Chapter 5 An explanation of the impedance of a piezoelectric bonded structure and experimental examples.

Chapter 6 Conclusion of the work and suggestions for future work will be given.

Chapter 2 Derivation of Mathematical Model

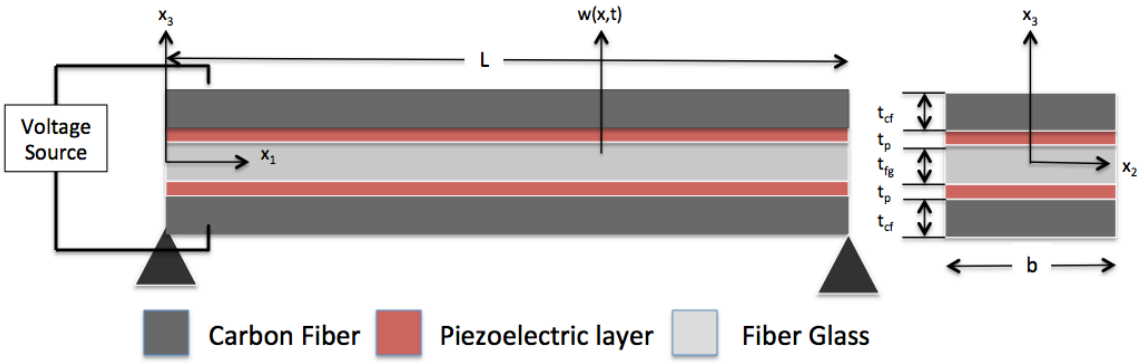

Figure 3. Bimorph piezoelctric beam

In order to approximate the dynamic response of ZnO nanowire embedded composites, a mathematical model of a bimorph piezoelectric beam was developed using Bernoulli-Euler beam theory and discretized using_the Galerkin method of weighted residuals. The beam model was based on the configuration shown in Figure 3.

2.1 Model Assumptions

For the purpose of simplifying the mechanics of the beam, the following assumptions were applied:

1. The length of the beam was much larger than the width, so Euler-Bernoulli conditions apply.
    a. Plane sections remain plane and perpendicular to the neutral axis
    b. Deformations due to shear are ignored
2. The thickness of the piezoelectric layer is much smaller than that of other layers
3. All layers of the beam are perfectly bonded to each other
4. Subject to small deformations, the beam exhibits linear-elastic behavior
5. The piezoelectric layers are poled in the x_3 direction

2.2 Hamilton's Principle

The key characteristic of piezoelectric materials is their electromechanical coupling. The constitutive equation for piezoelectric electromechanical coupling is given as [15, 44]:

$$\begin{bmatrix} \tau_{ij} \\ E_i \end{bmatrix} = \begin{bmatrix} C^D_{ijkl} & -h_{kij} \\ -h_{ikl} & \beta^S_{ik} \end{bmatrix} \begin{bmatrix} \varepsilon_{kl} \\ D_k \end{bmatrix} \tag{1}$$

where τ_{ij} is the stress tensor, C^D_{ijkl} is the elastic stiffness tensor under constant electric displacement, h_{kij} and h_{ikl} are the piezoelectric constants acting in their given directions, ε_{kl} is the strain tensor, E_i is the Electrical field per unit length, β^S_{ik} is the dielectric impermittivity under constant strain acting in its given direction, and D_k is the electrical displacement per unit length. Using this equation and Hamilton's Principle, shown below, the equations of motion of a bimorph composite beam can be derived.

$$\int_{t_1}^{t_2} [\delta T_b - \delta U_b - \delta U_c - \delta W_V] dt = 0 \tag{2}$$

Here T_b is the kinetic energy of the beam given as,

$$T_b = \int_0^L \rho_b A_b \dot{w}^2 \, dx \tag{3}$$

U_b is the strain energy of the beam given as,

$$U_b = \frac{1}{2} \int_0^L E_b I_b w_{xx}^2 \, dx \tag{4}$$

U_c is the electrical and mechanical energy of the piezoelectric layer given as,

$$U_c = \frac{1}{2} \int_0^L \left(2\tau\varepsilon + E_{v1} D_1 + E_{v2} D_2 \right) dV \tag{5}$$

δW_V is the virtual work given as,

$$\delta W_V = \int_0^L \left[V_1(t) b \delta D_1 + V_2(t) b \delta D_2 - c_b \dot{w} \delta w \right] dx \tag{6}$$

where ρ_b is the density of the beam, A_b is the cross-sectional area of the beam, E_b is the Young's Modulus of the beam, I_b is the cross sectional moment of inertia of the beam, E_{v1} and E_{v2} are the electrical fields under constant voltage of the top and bottom piezoelectric layers respectively, V(t) is the applied voltage, c_b is the damping coefficient, b is the width of the beam, and w is the deflection of the beam. Also, subscript 1 and 2 denote the top and bottom piezoelectric layers respectively, subscript x denotes the a spatial derivative with respect to x, and a dot over a variable denotes the time derivative of that variable [45].

Substituting equations (3-6) into (2) and simplifying yields the three governing equations (7-9)

$$\rho_b A_b \frac{\partial^2 w}{\partial t^2} + c_b \frac{\partial w}{\partial t} + E_b I_b \frac{\partial^4 w}{\partial x^4} + 2 I_p C_{11}^D \frac{\partial^4 w}{\partial x^4} + h_{31} J_p \left(D_1''(x) + D_2''(x) \right) \tag{7}$$

$$V_1(t) - \frac{h_{31} J_p}{b_p} \frac{\partial^2 w}{\partial x^2} + \frac{2\beta_{33}^S \left(h_p - h_b \right)}{b_p L} Q_1(x) \tag{8}$$

$$V_2(t) - \frac{h_{31} J_p}{b_p} \frac{\partial^2 w}{\partial x^2} + \frac{2\beta_{33}^S \left(h_p - h_b \right)}{b_p L} Q_2(x) \tag{9}$$

where C^D_{11} is the elastic modulus of the piezoelectric layer at constant electric displacement, J_b is the first moment of area of the piezoelectric layer, and Q is the charge.

$$Q(t) = \left(\frac{b_p L}{2\beta_{33}^S \left(h_p - h_b \right)} \right) \left(\frac{h_{31} J_p}{b_p} \frac{\partial^2 w}{\partial x^2} - V(t) \right) \tag{10}$$

$$D = \frac{Q}{b_p L} \tag{11}$$

$$\rho_b A_b \frac{\partial^2 w}{\partial t^2} + c \frac{\partial w}{\partial t} + E I_b \frac{\partial^4 w}{\partial x^4} + 2 I_p C_{11}^D \frac{\partial^4 w}{\partial x^4} + \frac{h_{31}^2 J_p^2}{2\beta_{33} b \left(h_p - h_b \right)} \frac{\partial^4 w}{\partial x^4} + \frac{2 h_{31} J_p}{\beta_{33} \left(h_p - h_b \right)} \frac{\partial^2 V(x,t)}{\partial x^2} = 0 \tag{12}$$

Equations (8) and (9) can be rewritten as (10) and plugged into (11) giving the form required to substitute into (7)* to give a single governing equation (12) where the following boundary conditions apply.

$$w(x) = 0 \qquad \text{at x = 0, L} \qquad (13)$$

$$\frac{d^2 w(x)}{dx^2} = 0 \qquad \text{at x = 0, L} \qquad (14)$$

2.3 Discretization using Galerkin's Method

Galerkin's Method is a weighted residual method of discretizing differential equations to find an approximate solution, given as:

$$Y^{(n)}(x) = \sum_{j=1}^{n} a_j \phi_j(x) \qquad (15)$$

where ϕ_j are the trial functions and a_j are their undetermined coefficients[46].

$$\phi_n(x) = \sin\left(\frac{n\pi x}{L}\right) \qquad (16)$$

Using the mass normalized eigenfunctions of a simply supported Euler-Bernoulli beam (16) and the boundary conditions (13, 14), equation (12) can be discretized into a set of decoupled ordinary differential equations,

---

* After plugging (11) into (7), terms describing the coupled displacement and voltage of the top and bottom of the beam appear. In order to consolidate them, the following continuity conditions are applied:

1) Change in deflection on top of beam = Change in deflection on bottom of beam with respect to x i.e., $\frac{d^4 w_1(x)}{dx^4} = \frac{d^4 w_2(x)}{dx^4}$

2) Change in Voltage on top Layer = Change in Voltage on bottom layer with respect to x i.e., $\frac{d^2 V_1(x,t)}{dx^2} = \frac{d^2 V_2(x,t)}{dx^2}$

$$M_{ij}\ddot{\eta}_i + C_{ij}\dot{\eta}_i + K_{ij}\eta_i + A_i V(t) = 0 \tag{17}$$

where

$$M_{ij} = \int_0^L \rho_b A_b \phi_i \phi_j \, dx \tag{18}$$

$$C_{ij} = \int_0^L c\phi_i \phi_j \, dx \tag{19}$$

$$K_{ij} = \int_0^L \left(E_b I_b + C_{11}^D I_p + \frac{h_{31}^2 J_p^2}{2\beta_{33}^S b\left(h_p - h_b\right)} \right) \phi_i'' \phi_j'' \, dx \tag{20}$$

$$A_i = \int_o^L \frac{h_{31} J_p}{\beta_{33}^S \left(h_p - h_b\right)} \phi_i'' dx \tag{21}$$

where M_{ij} is the mass matrix, C_{ij} is the damping matrix, K_{ij} is the stiffness matrix, and A_i is the amplitude of the input. Equation (17) can be rearranged in terms of natural frequencies of the system.

$$\ddot{\eta} + 2\zeta\omega_{ni}\dot{\eta} + \omega_{ni}^2 \eta = F \tag{22}$$

where

$$\omega_{ni} = \sqrt{\frac{K_{ij}}{M_{ij}}} \tag{23}$$

$$\zeta = \frac{C_{ij}}{2\sqrt{K_{ij} M_{ij}}} \tag{24}$$

$$F = \frac{A_i}{M_{ij}} V\left(t\right) \tag{25}$$

where ω_{ni} are the natural frequencies of the system and ζ is the damping ratio for the beam.

2.4 Frequency Response

In order to compare the theoretical calculations to laser vibrometry data, the results must be converted from the time to frequency domain. This is accomplished by taking the Laplace transform of Equation (22), which gives the following.

$$\left(s^2+2\zeta\omega_{n_i}s+\omega_{n_i}^2\right)\eta_i(s)=FV(s) \tag{26}$$

This can be rewritten as the ratio of output to input values and substituting jω for s (where j is √-1) gives the transfer function $G_i(j\omega)$, or as the transfer function with velocity as output $G_i^*(j\omega)$.

$$G_i(j\omega)=\frac{\eta_i(j\omega)}{V(j\omega)}=\frac{\frac{A_i}{M_i\omega^2}}{\left(\frac{\omega_{n_i}}{\omega}\right)^2-1+2j\zeta\frac{\omega_{n_i}}{\omega}} \tag{27}$$

$$G_i^*(j\omega)=\frac{\dot{\eta}_i(j\omega)}{V(j\omega)}=\frac{\frac{jA_i}{M_i\omega}}{\left(\frac{\omega_{n_i}}{\omega}\right)^2-1+2j\zeta\frac{\omega_{n_i}}{\omega}} \tag{28}$$

The frequency response of the i^{th} vibrational mode is displayed as the absolute value of (28) vs frequency.

Chapter 3 Fabrication and Experimentation

3.1 Sample Fabrication

Zinc Oxide nanowires were fabricated in Dr. Marwan Al-Haik's lab in the Virginia Tech's Department of Engineering Science and Mechanics. The nanowires were embedded in composite laminates to investigate their ability to create smart composites with electromechanical coupling characteristics. Two 130 mm x130 mm squares of plain-woven fiberglass (FG) were cut for ZnO nanowire growth. The plies were then sputtered on both sides with an 80 nm layer of ZnO using AJA international inc.'s OTC Orion high vacuum magnetron sputtering system, under a 3 mTorr vacuum argon atmosphere and 300 Watts of power from an RF source. 40 mmol of 99% pure Sigma-Aldrich, Inc. Zinc acetate hexahydrate – $Zn(O_2CCH_3)_2(H_2O)_2$ – and Hexamethyl-lenetetramine (HMTA) – $(CH_2)_6N_4$ – were dissolved in deioninzed (DI) water and heated to 85 °C. The ZnO sputtered FG was submerged in the Zinc acetate HMTA solution for 8 hours. The FG was then removed and rinsed with DI water and left to dry overnight in an 85 °C oven. Figure 4 shows an SEM micrograph of the ZnO nanowires after growth on the FG using a 5200 Hitachi FE-SEM electron microscope operating at 5 kV.

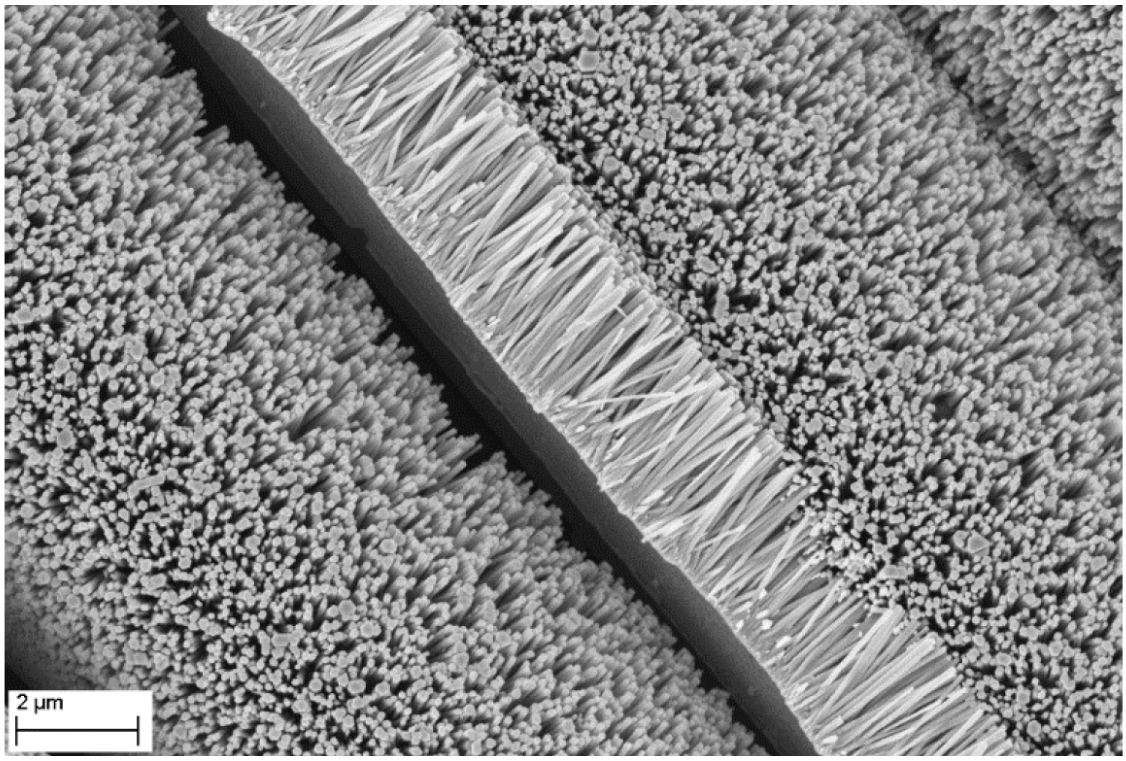

Figure 4. SEM micrograph of ZnO nanowires grown on fiberglass

The two plies of ZnO grown FG were stacked together and a ply of plain-woven carbon fiber (CF) of the same size was placed on either side of the FG layer so that a layup of [CF/FG/FG/CF] resulted. PTM&W Industries Inc. Aeroppoxy^{TM} was applied to the fabric using hand layup and then cured in a press under vacuum with 25 tons of applied force at 65 °C for four hours. Samples were then postcured for two hours at 90 °C to ensure complete curing of the matrix resin. After curing, they were cut to size.

The laminate's surface was scratched to allow for a connection to the CF layer. Wires were then attached to CF using silver conductive epoxy. A finished composite sample is shown in Figure 5.

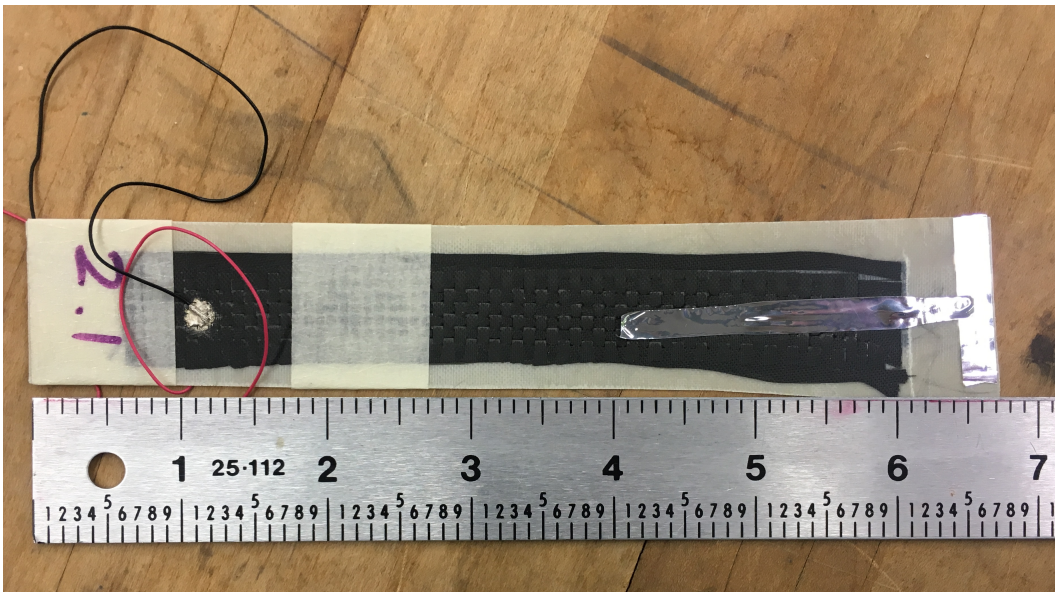

Figure 5. ZnO nanowire embedded composite (Sample 2.1)

3.2 Experimental Setup

ZnO laminate samples were tested in Virginia Tech's Aerospace Structures and Materials Lab (ASML). Laser vibrometry tests were performed using a Polytec laser vibrometer to measure the tip velocity of the laminate, a National Instruments (NI) system with a PXI-4461 (24-Bit, 204.8 kS/s, 2-Input/2-Output), and a PXI-4462 (24-Bit, 204.8 kS/s, 4-Input) to generate an electrical excitation and record the excitation frequency and deflection velocity. Samples were attached to the NI system and excited on a frequency range of 0 – 1000 Hz using two different configurations: simply supported where the samples were excited while being laid flat on a table and cantilever where the end of the sample with the attached leads was clamped into a LDS V408 vibration shaker that was not powered on, seen in Figure 6. Their tip velocity was measured at a sampling rate of 2000 samples per second. A low pass filter of 100 kHz was applied.

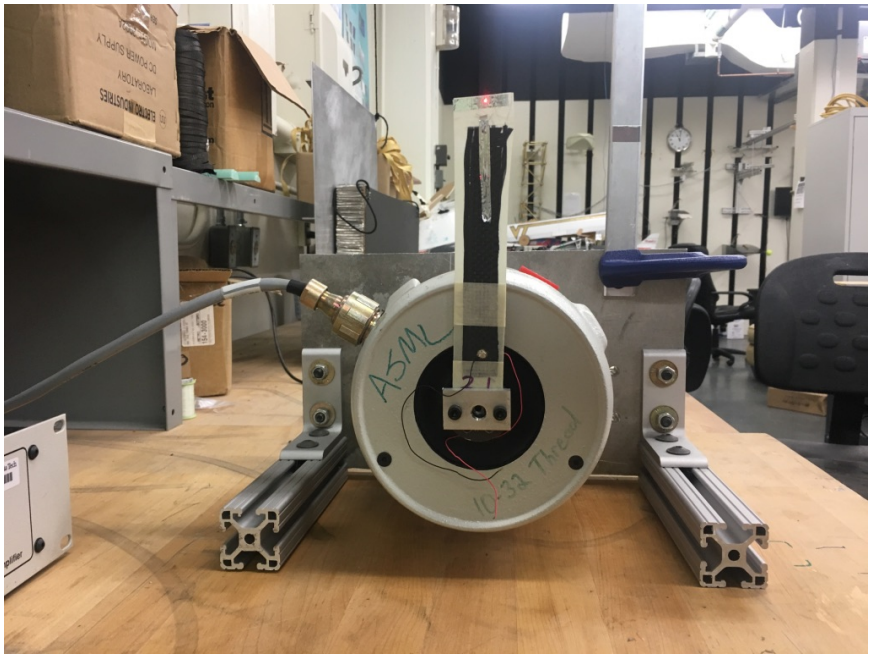

Figure 6. Cantilever Test Configuration

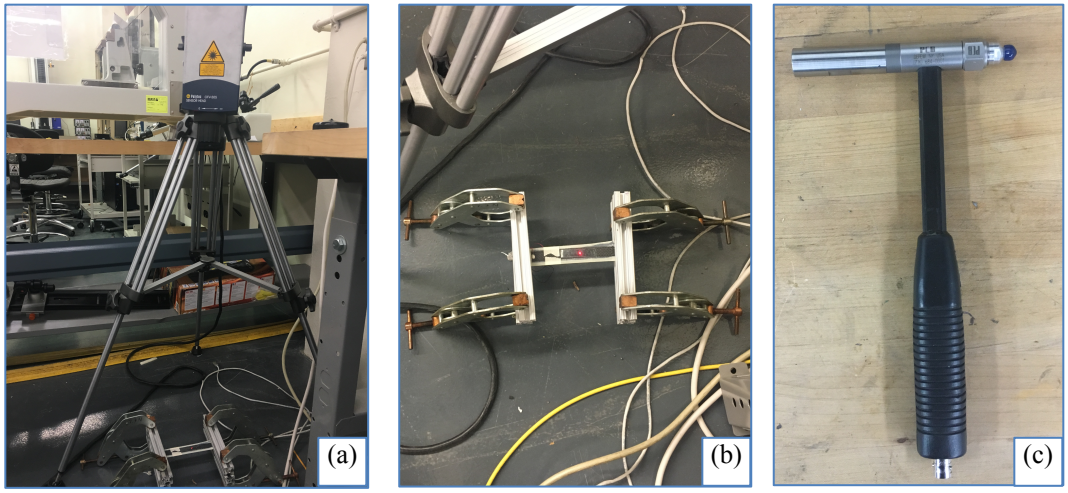

Figure 7. a) Experimental Setup (b) clamped beam (c) impact hammer

The samples were also tested in a clamped-clamped arrangement where the velocity was measured at the mid-length of the laminate after it was struck with a PCB 086C03 general-purpose modal analysis impact hammer. This configuration is shown in Figure 7.

Chapter 4 ZnO Beam Experiment and Analysis Results

Clamped-Clamped (C-C) impact hammer tests were performed to find the natural frequencies of the beam. Raw data from three separate tests on Sample 2.1 were run through a loess weighted regression filter with a weight of 0.01. Natural frequencies for the beam were at local maxima along the resulting filtered plot. Results from the test are shown in Figure 8 and Table 1.

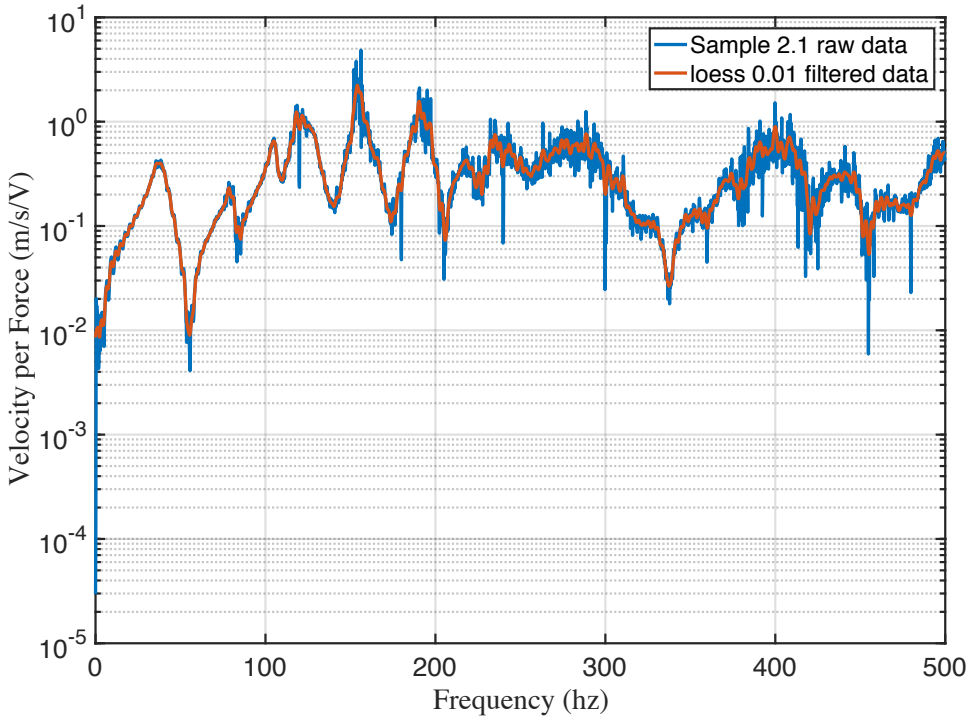

Figure 8. Sample 2.1 Clamped - Clamped Vibration Results

These estimated natural frequencies taken from experimentation can be compared to the theoretical natural frequencies of a Clamped – Clamped Sample 2.1, using Equation (29),

$$\omega_{n_i} = \beta_i^2 \sqrt{\frac{EI}{mL^3}} \tag{29}$$

where β_i is a constant for the i^{th} vibrational mode of the beam, that is derived from the beam equation, Equation (30), and the beam's boundary conditions [47].

$$X = C_1 \sin(\beta x) + C_2 \cos(\beta x) + C_3 \sinh(\beta x) + C_4 \cosh(\beta x) \tag{30}$$

Table 1. Natural Frequency and Velocity Measurements for Clamped Beam

Test	Value	1	2	3	4	5	6	7
1	ω_n (Hz)	37.2	77	103.6	122.2	155	191	216
	Magnitude (mm/s/V)	4.3	3.9	4.4	4.8	5	4.8	4.3
2	ω_n (Hz)	40.8	91	131.6	177	223.4	268.8	308
	Magnitude (mm/s/V)	4	4.3	4.4	4.5	4.3	4.7	3.9
3	ω_n (Hz)	40.4	83.8	104	126	165	202	232.8
	Magnitude (mm/s/V)	4.3	4.6	4.7	4.8	4.6	4.6	4.5
Average	ω_n (Hz)	39.5	83.9	113.1	141.9	181.1	221.1	252.5
	Magnitude (mm/s/V)	4.2	4.3	4.5	4.7	4.6	4.7	4.3

The first three theoretical natural frequencies for sample 2.1 clamped at both ends are shown in Table 2.

Table 2. Theoretical Natural Frequencies of Clamped-Clamped Beam 2.1

Natural Frequency	1	2	3
ω_n (Hz)	28.8555	79.5426	155.9353

When comparing Table 2 to the average natural frequencies from Table 1, the two sets of frequencies are very close to each other, and strongly suggest that local maxima observed in Figure 8 correspond to the natural frequencies of the beam.

Similar experimentation was run with one sample in a cantilever configuration as well as six separate samples which were laid flat on a table. The samples were excited with an applied voltage, and their tip velocities were measured to obtain the natural frequencies of the beams. The results are shown in Figure 9 and Table 3, and Figure 10 and

Table 4

for the cantilever and free configurations respectively. Due to weak electromagnetic coupling, there was significant noise in Figure 9 and Figure 10, so a filtered curve of the data is also displayed in the figures.

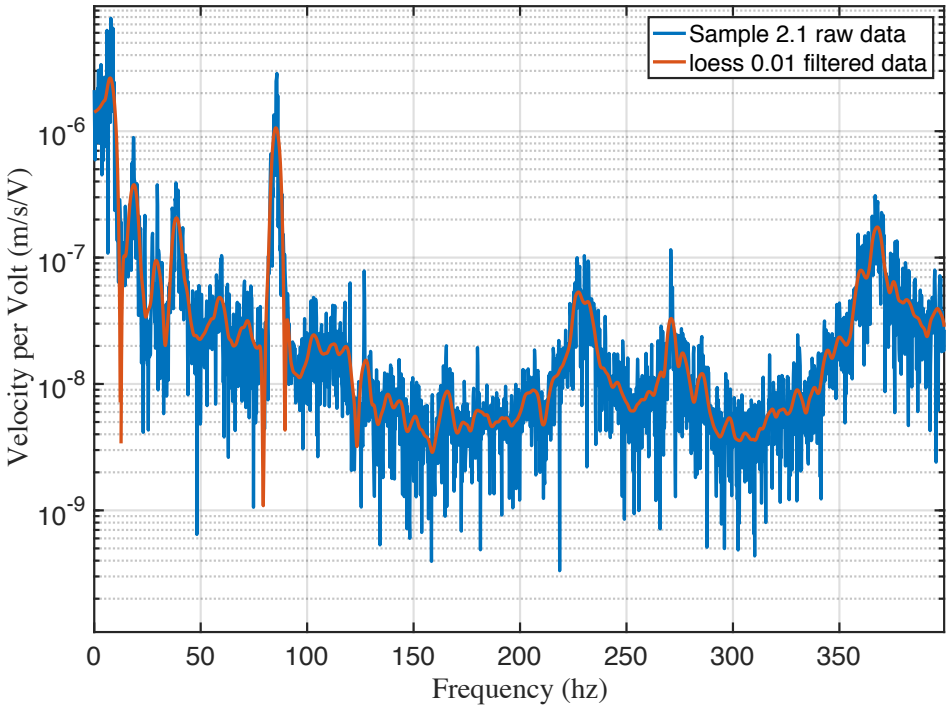

Figure 9. Sample 2.1 Cantilever Vibration Under Electrical Excitation

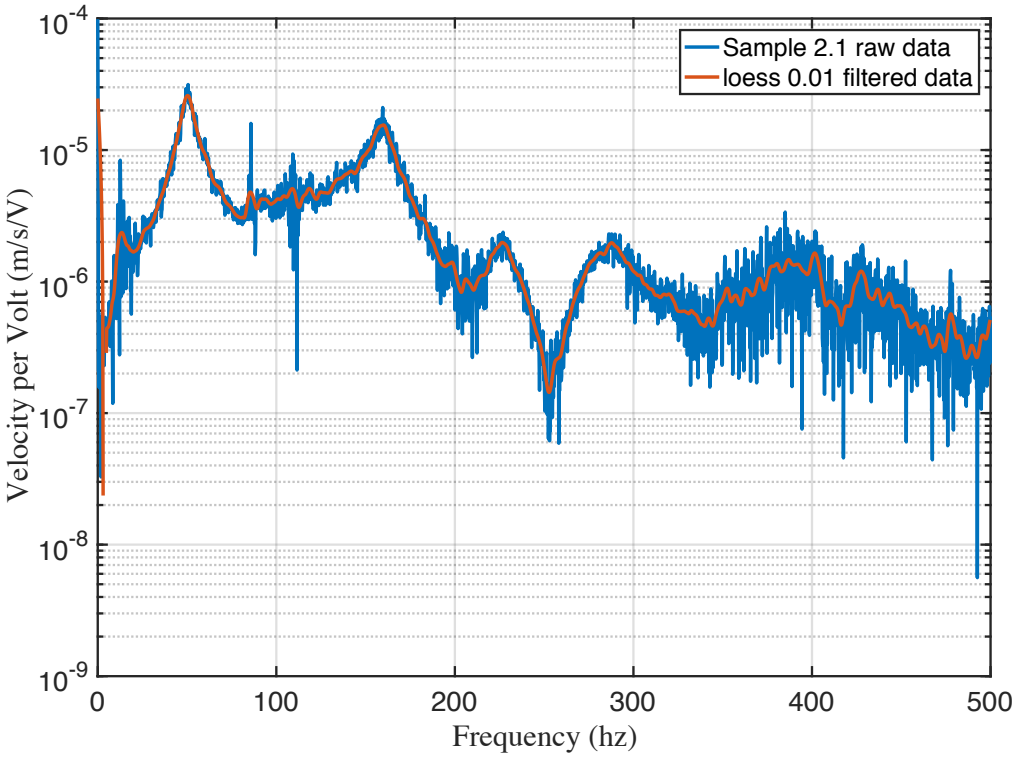

Figure 10. Sample 2.1 Free-Free Vibration under Electrical Excitation

Table 3. Natural Frequencies and Magnitude Measurements for Sample 2.1 as a Cantilever beam

Test	Value	1	2	3
1	ω_n (Hz)	7.6	18.6	85.2
	Magnitude (m/s/V)	2.636 E-6	3.77 E-7	1.063 E-6
2	ω_n (Hz)	7.8	18.2	85
	Magnitude (m/s/V)	1.837 E-6	3.08 E-7	6.34 E-7
3	ω_n (Hz)	7.6	18.8	85.4
	Magnitude (m/s/V)	4.159 E-6	4.98 E-7	1.314 E-6

Table 4. Natural Frequencies and Velocity Measurements for Free Beams

Sample	Value	1	2	3	4	5	6	7
2.1	ω_n (Hz)	13.4	50.4	81	85.4	92	93.8	101
	Magnitude (10^{-5} mm/s/V)	0.236	02.60	0.308	0.479	0.425	0.424	0.425
2.3	ω_n (Hz)	6	12.8	17.6	23.2	29.6	36.6	41
	Magnitude (10^{-5} mm/s/V)	0.0292	0.206	0.149	0.0761	0.0599	0.0645	0.150
2.4	ω_n (Hz)	5.8	12.4	18.4	23.2	29.4	36.4	41.4
	Magnitude (10^{-5} mm/s/V)	0.0137	0.195	0.1332	0.0558	0.0573	0.110	0.153
2.5	ω_n (Hz)	5	12.2	18	23.6	27.8	36.2	41.2
	Magnitude (10^{-5} mm/s/V)	0.0260	0.268	0.1425	0.0556	0.0737	0.0620	0.0755
2.6	ω_n (Hz)	6.2	12.4	17.8	20.2	23.4	28.2	34.4
	Magnitude (10^{-5} mm/s/V)	0.0254	0.171	0.0859	0.0835	0.0808	0.1001	0.0961
2.7	ω_n (Hz)	6	12.4	18.6	25.6	36.4	41	48.2
	Magnitude (10^{-5} mm/s/V)	0.0208	0.152	0.131	0.0667	0.0798	0.0610	0.0634

Natural frequencies from Table 3 were used to construct graphs of the frequency response of the beam, shown in Figure 11. Similar to the C-C configuration from earlier, local maxima in the experimental data from Figure 11 correspond to peaks in the frequency response which occur at the natural frequencies of the observed structure. The frequency response is calculated by summing the absolute values of Equation (28) for each natural frequency of interest. For example, the frequency response of Sample 2.1 as a cantilever beam, shown in Figure 11, has three natural frequencies of interest, row 1 from Table 3. These three natural frequencies were used to calculate a G^*_1, G^*_2, and G^*_3 respectively from Equation (28), whose absolute values were then summed together to generate a frequency response function. Because the natural frequencies used to create the frequency response

were taken directly from the peaks that occur in the experimental data, the peaks of the frequency response occur at the same exact frequency as their corresponding peaks in Figure 11. This "experimental" frequency response from Figure 11, can be compared to a truly theoretical one that is based off of the theoretical natural frequencies of the beam. These natural frequencies are calculated according to Equation (29). Figure 12 shows a comparison of the frequency responses for natural frequencies from the experimental data and theoretical calculations. It is of note that discrepancies between the experimental and theoretical natural frequencies shown in the figure could be due to the weak electromechanical coupling of the beam and noise in the data. However, there appears to be a good agreement between the two sets of data on the location of the first natural frequency.

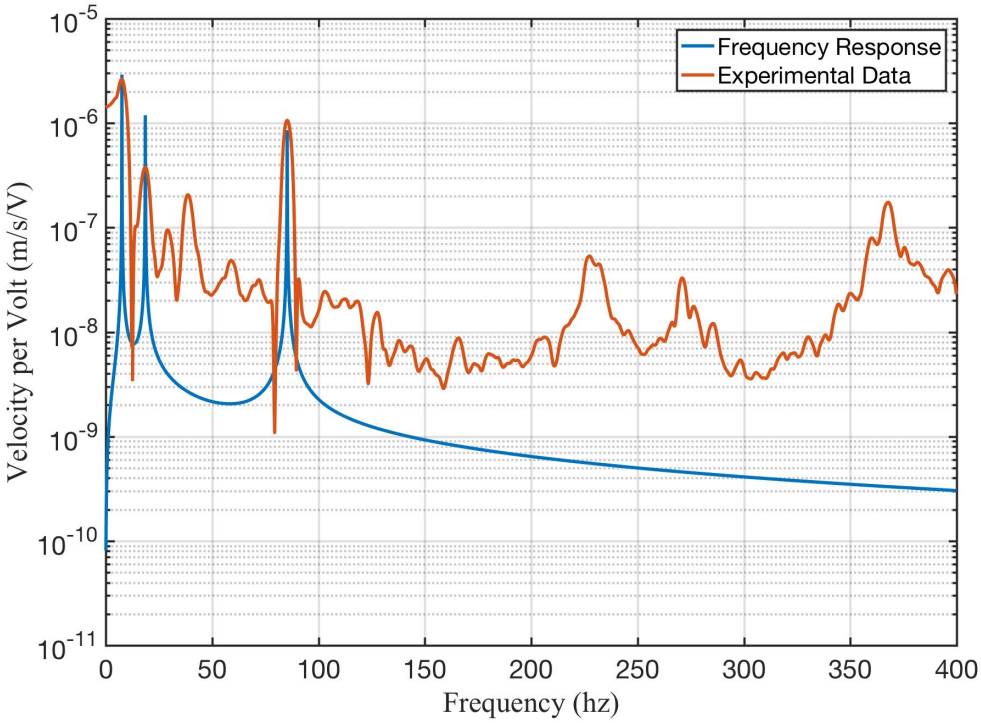

Figure 11. Frequency Response of Cantilevered Beam 2.1

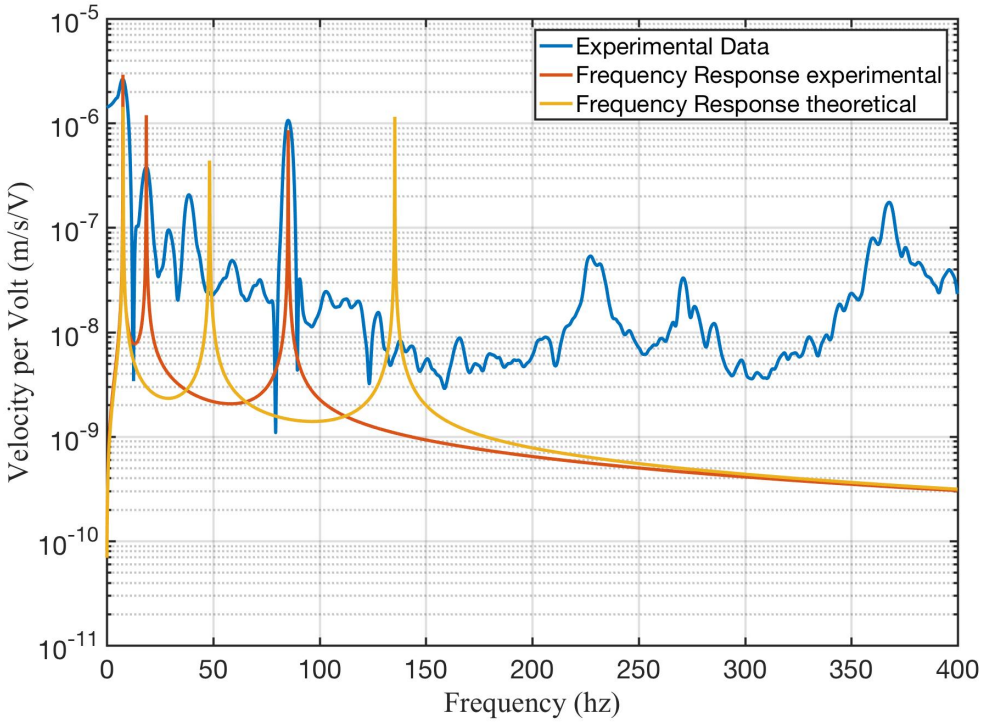

Figure 12. Comparison of frequency responses derived from theoretical and experimental natural frequencies

The magnitudes and frequencies of the peaks from the experimental frequency response from Figure 11 were then used to obtain an approximation for the piezoelectric constants. This was achieved by inserting Equations (18) and (21) into Equation (28) and solving for h_{31} with the frequency equal to the natural frequency of interest, i.e. the natural frequencies from the experimental frequency response, which results in Equation (31).

$$h_{31_i} = \frac{\beta_{33}^S \left(h_p - h_b\right) M_i L \omega_{n_i} \zeta}{2 J_p \pi} \left| G_i^* \left(j\omega_{n_i} \right) \right| \tag{31}$$

The dielectric constant for the piezoelectric layers was estimated from experimental work performed by Yang et al. [48]. Yang examined the effect of ZnO nanowire diameter on the dielectric constant of the nanowire, shown in Figure 13 [48].

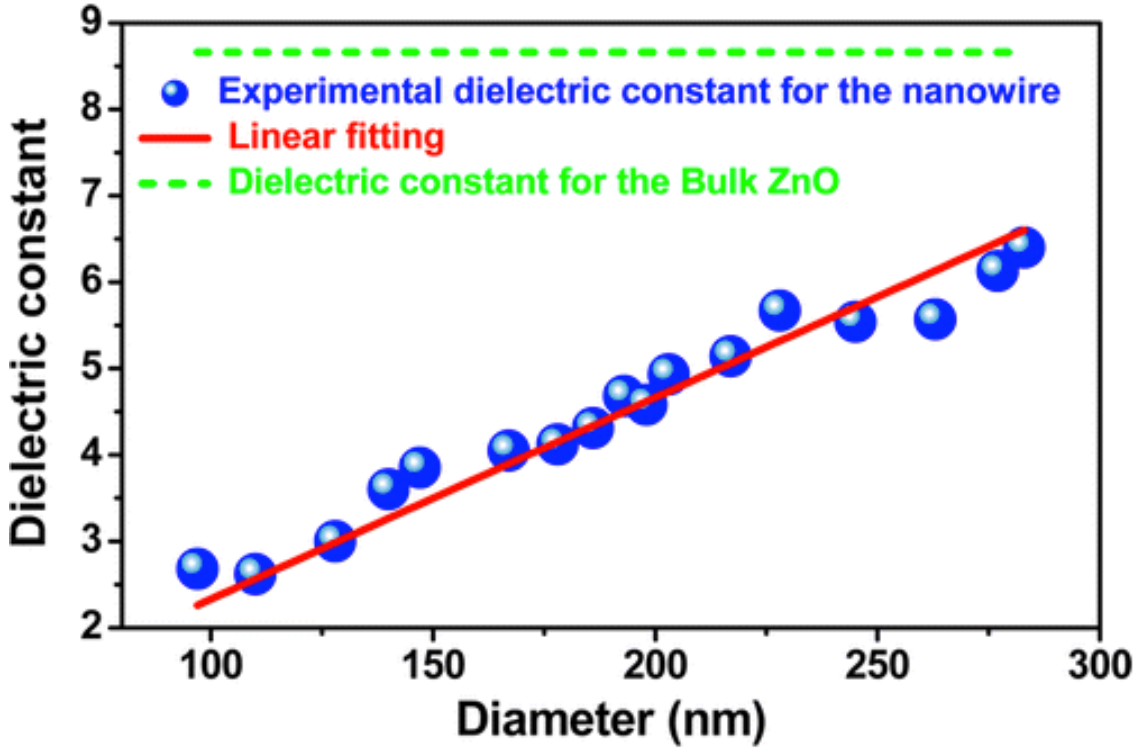

Figure 13. Dielectric Constants of ZnO Nanowire with varying diameter [48]

Using a nanowire diameter of 200 nm, as reported by Dr. Al-Haik and his team, the impermittivity of the piezoelectric layer, β^S_{33}, is found by means of Equation (32),

$$\beta^S_{33} = \frac{1}{\varepsilon^S_r \varepsilon_0} \tag{32}$$

where ε^S_r is the dielectric constant under constant strain and ε_0 is the permittivity of free space. Piezoelectric constant h_{31} can then be calculated by using the magnitude of the frequency response at selected natural frequencies, given in Table 2 and 3, for $|G_i^*(j\omega)|$ in Equation (31).

Piezoelectric constant h_{31} is useful for this model but is not a commonly used value for commercial products, which prefer constants d_{31}, the piezoelectric charge constant, or g_{31}, the piezoelectric voltage constant. In order to find these values, the constants β^T_{33}, c^D_{11} are required. Here, C^D_{11} is the Young's modulus of the piezoelectric layer at constant electrical pressure, as defined in Chapter 2, and β^T_{33} is the impermittivity of the piezoelectric layer at constant stress.

$$\beta_{33}^{T} = \beta_{33}^{S} - g_{31} h_{31} \tag{33}$$

$$g_{31} = \frac{h_{31}}{C_{11}^{D}} \tag{34}$$

$$d_{31} = \frac{h_{31}}{\beta_{33}^{T} C_{11}^{D}} \tag{35}$$

Similar to β^{S}_{33}, c^{D}_{11} is also diameter dependent. Chen et al. experimentally estimated the young's modulus of ZnO nanowires over a range of nanowire diameters, seen in Figure 14 [49]. With the experimentally obtained modulus for the nanowires, β^{T}_{33}, d_{31}, and g_{31} can be easily found using Equations (33-35), shown above. Results are tabulated and compared to commercially available products from Measurement Specialties, Inc. and APC International, Ltd. in Table 5.

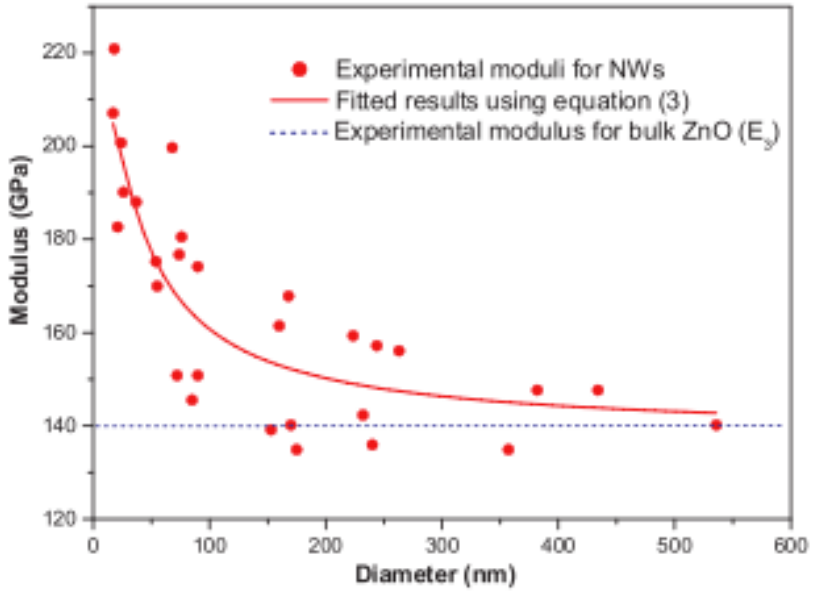

Figure 14. Young's Modulus of ZnO nanowire as a function of nanowire diameter [49]

Table 5. Piezoelectric Constants

Constants	ZnO NW	PZVDF Film	APC 850	APC 855
h_{31} (10^{8} V/m)	0.9138	4.34	7.812	5.31
g_{31} (10^{-3} Vm/N)	0.6092	216	12.4	9
d_{31} (10^{-12} m/V)	0.0246	23	175	276

As seen in Table 5, the theoretical piezoelectric constants of the ZnO NWs are significantly lower than that of the commercially available piezoelectric products. These low piezoelectric coefficients result in low piezoelectric coupling for the test samples. Due to the low coupling of the test beams, it is unclear if the peaks shown in Figures 8-12 correspond to natural frequencies of the beam.

When calculating the piezoelectric constants, the piezoelectric layer is assumed to have a 100% volume fraction so that the entire layer is made up of only piezoelectric material. However, in reality there is some degree of matrix that fills in any gaps between nanowires. Since the nanowire volume fraction is unknown, Figure 16 and Figure 17 show the variance in piezoelectric constants with respect to ZnO nanowire volume fractions.

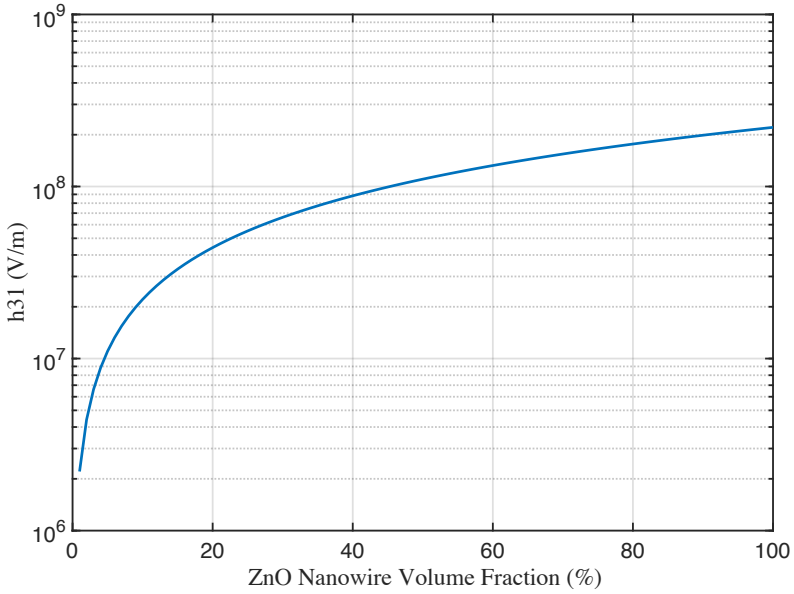

Figure 15. Effect of ZnO Volume Fraction on Piezoelectric Constant h_{31}

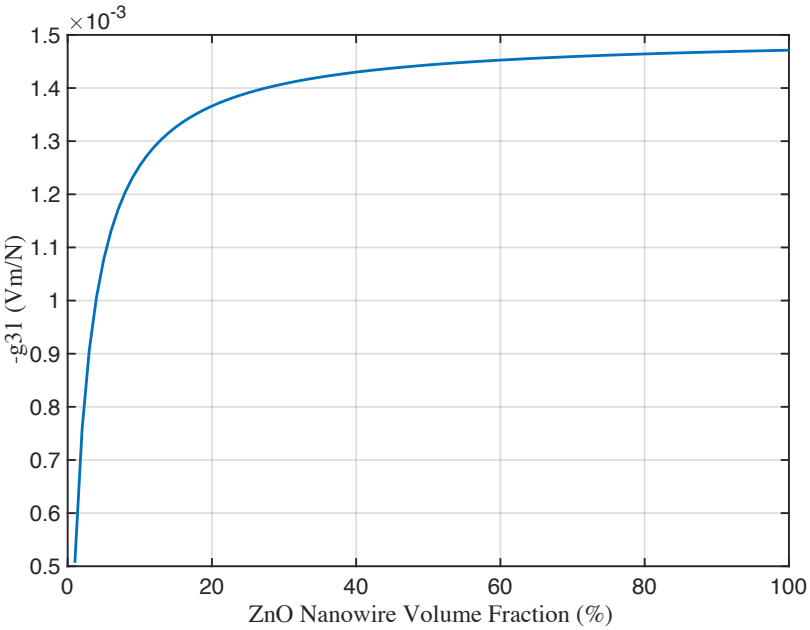

Figure 16. Effect of ZnO Volume Fraction on Piezoelectric Constant g_{31}

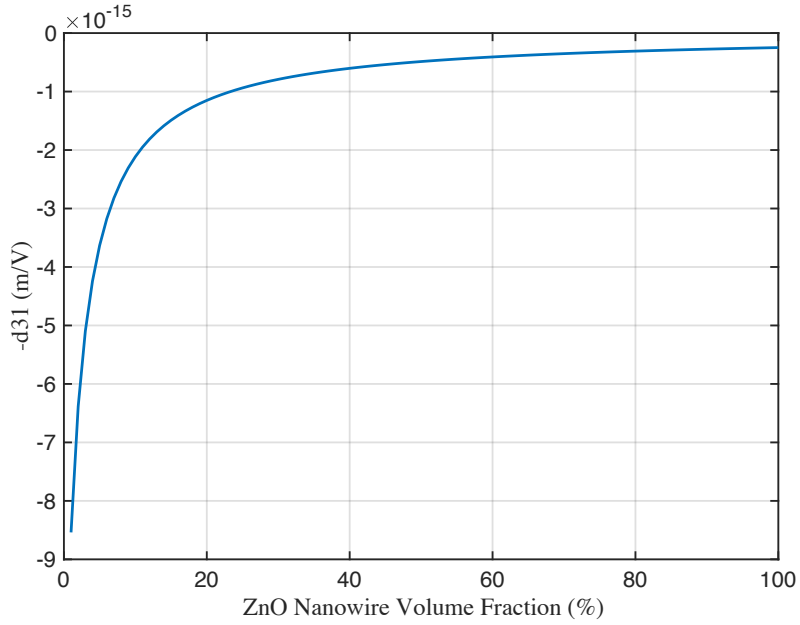

Figure 17. Effect of ZnO Volume Fraction on Piezoelectric Constant d_{31}

Piezoelectric constants d_{31} and g_{31} show a steep increase until about 15% volume fraction where their slope rapidly decreases until the volume fraction reaches 100%. This shows

that after about 20%, the effect of volume fraction of ZnO Nanowires on piezoelectric properties decreases until they approach those of the bulk piezoelectric material at 100%.

Chapter 5 Impedance based SHM

5.1 Motivation

Fiber reinforced composites that serve as load bearing members are susceptible to degradation of mechanical properties due to a process call delamination after frequent or over loading. In order to detect damage to the composites without damaging them, processes known as nondestructive evaluation (NDE) are utilized. Frequently used methods of NDE include computerized tomography (CT) scans and X-rays, which are expensive and time consuming and carry the risk of error since they rely on the evaluator's judgment and equipment. This creates the demand for smart materials with integrated damage detection capabilities, whose benefits could include: reduction of maintenance costs and time, improvements to structural reliability and safety, and prevention of catastrophic failure that could lead to loss of life. This sort of autonomous NDE is known as structural health monitoring (SHM).

One type of impedance based SHM relies on a series of bonded actuator sensors usually made of piezoceramic (PZT) patches or wafers. It relies on the electromechanical coupling of the PZT's electrical impedance, and a host structure's mechanical impedance, which was proven by Liang et al[50]. Through this coupling, changes in the mechanical impedance of the structure are capable of being measured by the change in electrical impedance of the sensor. Additional advantages of impedance based SHM include: low power requirements (under 1 Volt), ability for use with complex structures, and no need for an analytical model for implementation.

5.2 Impedance

5.2.1 Structural Impedance

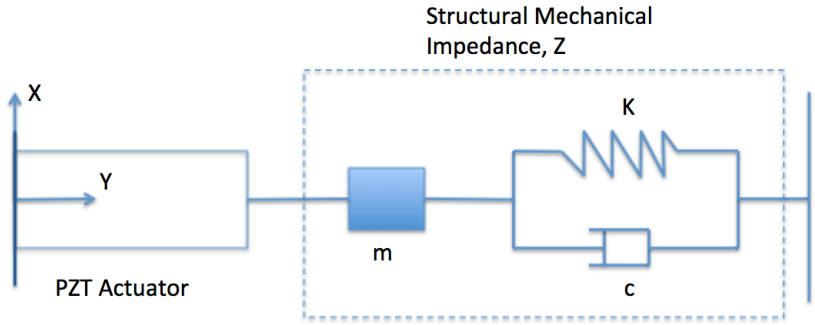

Figure 18. PZT actuated spring mass damper one degree of freedom system

The basis of Impedance Based Structural Health Monitoring is the electromechanical coupling of the electrical and structural impedances of a structure. Given the one degree of freedom spring mass damper system shown in Figure 18 [51], the structural impedance of the system is given by:

$$Z = c + m\frac{\omega^2 - \omega_n^2}{\omega}i \tag{33}$$

where Z is the structural impedance of the structure, i is $(-1)^{1/2}$, c is the damping coefficient, m is the mass of the system, ω is the dynamic frequency of the system, and ω_n is the natural frequency of the system given by:

$$\omega_n = \sqrt{\frac{k}{m}} \tag{34}$$

where k is the spring constant for the system [51].

5.2.2 Electrical Impedance

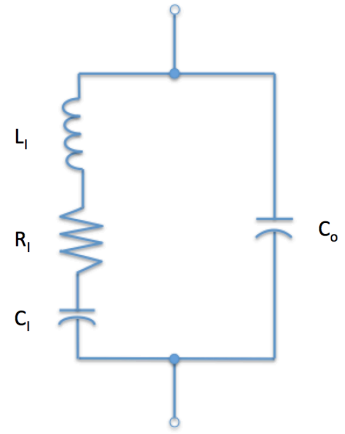

Figure 19. Equivalent Circuit of a Piezoelectric Structure

The equivalent electrical circuit is given in Figure 17, and is made up of an inductor, resistor, and a capacitor. The electrical impedance for this circuit is the inverse of the circuit's admittance, Y, given as:

$$Y = \frac{I}{V} = Y_0 + Y_P \tag{35}$$

where Y_0 and Y_P are given as:

$$Y_0 = j\omega C_0 \tag{36}$$

$$Y_P = j\omega C_0 \frac{\kappa_{12}^2}{1-k_{12}^2} \frac{\tan a}{a} \tag{37}$$

$$C_0 = \varepsilon_{11}^{LS} \frac{bl}{t} \tag{38}$$

$$\kappa^2 = \frac{d^2}{\varepsilon^T s^E} \tag{39}$$

$$a = \frac{1}{2} kl = \frac{\omega l}{2\upsilon} \tag{40}$$

where j is √-1, ω is the frequency, ε is the permittivity constant, d is the piezoelectric constant, s is the elastic compliance constant, ν is the applied voltage, l is the length of the piezoelectric structure, b is the width, and t is the thickness. Superscript E denotes

constant electrical field, superscript T denotes constant stress, and LS denotes lengthwise clamped [15].

5.2.3 Electro Mechanical coupling of Impedance

The electrical mechanical piezoelectric system shown in Figure 18 combines the systems shown in Figure 16 and Figure 17 so that the PZT is actuated by the applied voltage v(t). The electrical mechanical impedance for this system is given as:

$$Z(\omega)=\frac{1}{i\omega C}\left(1-\kappa_{31}^{2}\frac{k_{str}(\omega)}{k_{PZT}+k_{str}(\omega)}\right)^{-1} \tag{41}$$

where C is the capacitance of the PZT at no load, κ_{31} is the electro-mechanical cross coupling coefficient of the PZT, k_{str} is the stiffness of the structure, k_{PZT} is the stiffness of the piezoelectric structure[52].

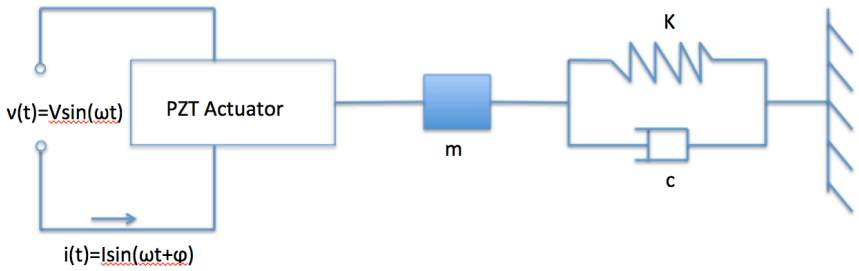

Figure 20. Electrical Mechanical PZT System

5.2.4 Structural Damage Metric

In order to introduce a statistical metric for damage evaluation, baseline impedance of the undamaged structure is compared to those of the structure after damage has incurred. The impedance measurements are taken over a frequency range, typically between 30-400 kHz, and evaluated using Root Mean Squared Deviation (RMSD):

$$M=\sum_{i=1}^{n}\sqrt{\frac{\left[\mathrm{Re}(Z_{i,1})-\mathrm{Re}(Z_{i,2})\right]^{2}}{\left[\mathrm{Re}(Z_{i,1})\right]^{2}}} \tag{42}$$

where Z_1 is the impedance of the undamaged structure, and Z_2 is the impedance of the structure for comparison. An increase in M represents an increase in the difference of the structure at times 1 and 2, implying an increase in damage to the structure[32, 53].

5.3 Experimental Setup

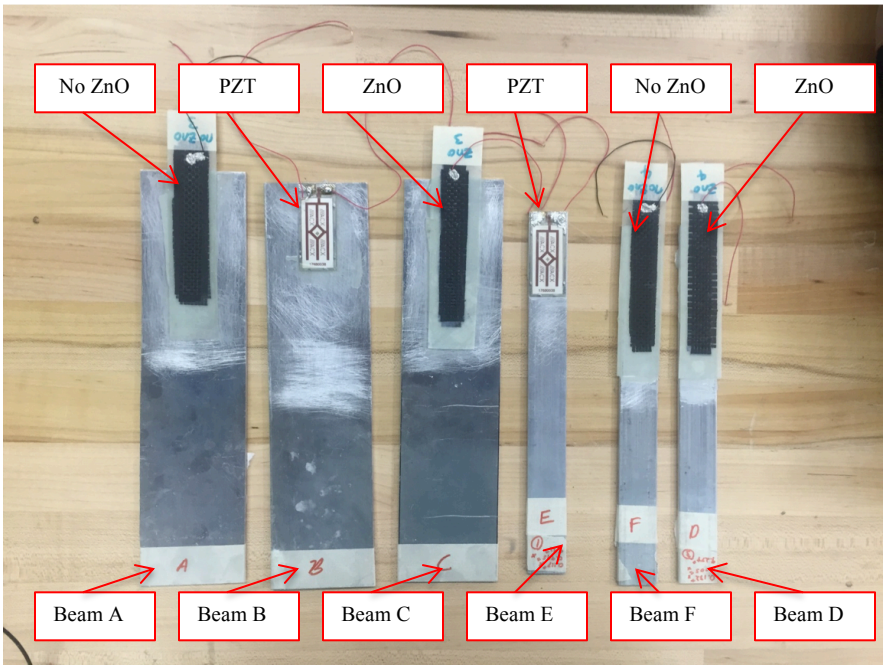

Figure 21. Composite and PZT bonded Al Beams

Carbon fiber composites with and without ZnO nanowires and Quik-Pak PZT patches were bonded to Al beams in order to observe their ability to demonstrate electromechanical coupling with the host structure. Two different Al beam configurations were used, one and two and a half inch wide beams, respectively.

Table 6. Experimental Sample Descriptions

Beam Name	A	B	C	D	E	F
Al Beam Size (in)	10.3 x 2.6	10.2 x 2.6	10.2 x 2.5	9.2 x 1	9.3 x 1	9.2 x 1
Bonded Sample	No ZnO Composite	Quick-Pak PZT	ZnO composite	ZnO Composite	Quick-Pak PZT	No ZnO Composite

Figure 21 shows the samples tested, and Table 6 lists their descriptions. Impedance of each of the bonded beams was taken using an Agilent E4980A Precision LCR Meter. After

the initial baseline impedance test was run, holes were drilled into the Al beam at 1" intervals. Impedance tests were performed after each new hole was introduced to the beam.

5.4 Results

After damage was introduced to the Al beams, an increase in the damage metric M was seen in the beams with bonded PZTs and ZnO embedded composites. There was no significant change in damage metric for the beams with composites attached that contained no ZnO. Figure 22 and Figure 23 show the increase in M as more holes were added to the beams.

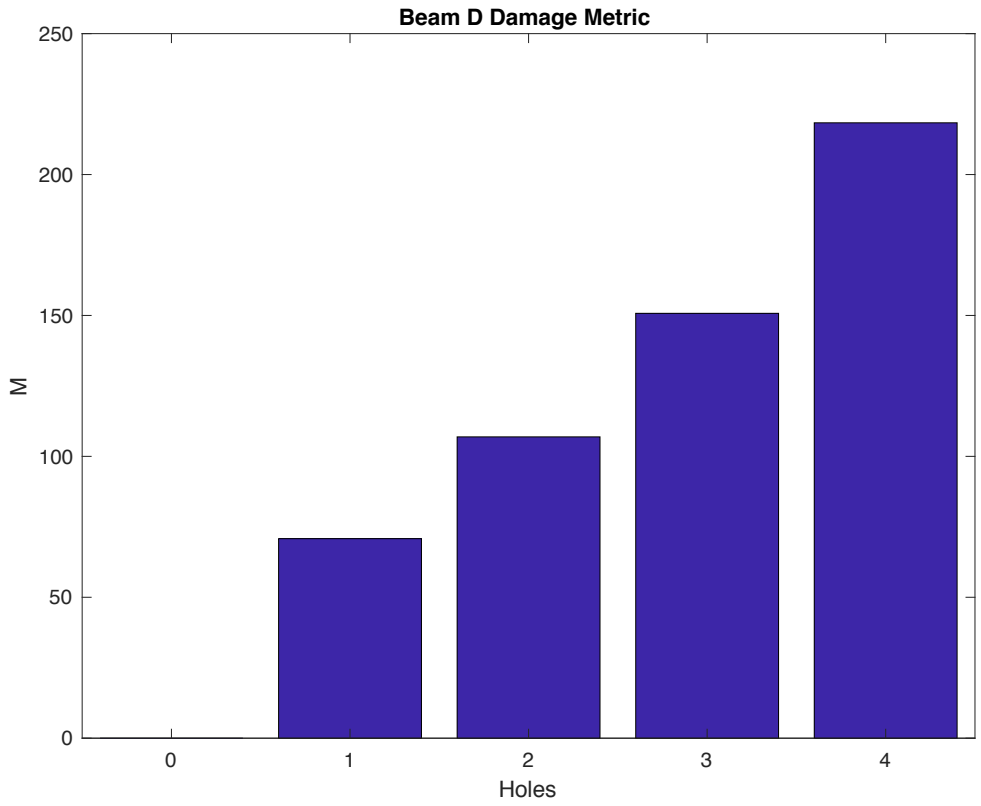

Figure 22. Beam D, Narrow Beam with ZnO Composite

As seen in Figure 22 and Figure 23, the damage metric for the beam with the PZT is an order of magnitude greater than that of the beam with the attached ZnO composite. This is as expected due to the weak piezoelectric coupling found in the composites, as discussed in the previous chapter.

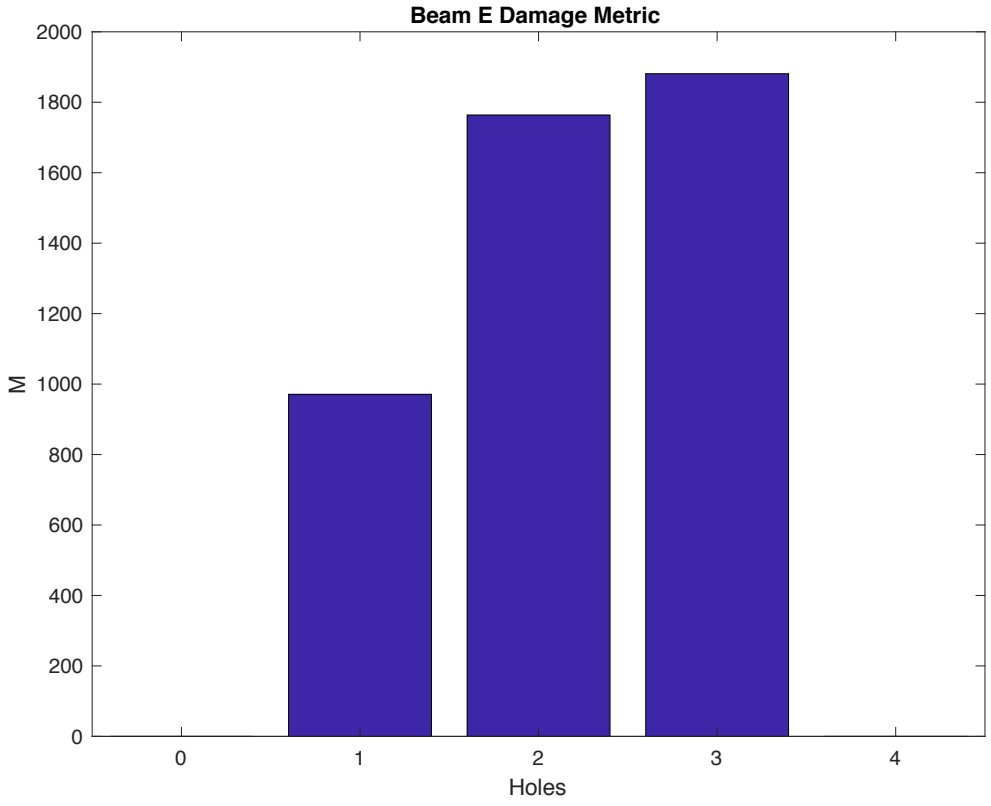

Figure 23. Beam E, Narrow Beam with PZT

These results show a consistent change in M corresponding to progressive damage that was introduced to the host structure. This implies that the ZnO imbedded composites are able to detect changes in their host structure's mechanical impedance due to their electromechanical coupling. For this reason, they are a promising material for impedance based structural health monitoring applications and should be examined further since they have the potential to act as host structures with integrated actuating and sensing capabilities.

Chapter 6 Conclusion

6.1 Summary of Work

In order to investigate the potential piezoelectric properties of ZnO nanowires embedded in a composite laminate, ZnO nanowires were sputtered onto both sides of a sheet of fiberglass, which was sandwiched between two pieces of plain woven carbon fiber, wetted with Aeroepoxy^{tm}, and cured in a press with 25 tons of pressure at 65 °C for four hours. After postcuring for two hours at 90 °C the samples were attached with electrical leads.

Samples were excited with an applied voltage over a frequency range from 0 to 1000 Hz in a simply supported and cantilever setup. Test results were filtered using a loess weighted regression with a weight of 0.01 so that potential natural frequencies could be identified at local maxima.

A dynamic model was derived using BE beam theory and discretized using Galerkin's method of weighted residuals. The magnitudes of these peaks, along with their locations were used along with the beam's theoretical natural frequencies to estimate the beam's piezoelectric constants. The effect of the ZnO's volume fraction in the beam on the beam's piezoelectric constants was examined by varying the volume fraction of the ZnO nanowires in the model.

The electromechanical coupling properties of ZnO nanowire embedded composite laminates was examined by observing their ability to transfer changes in the structural impedance of a host structure to changes in electrical impedance. Composite laminates with and without ZnO nanowires, as well as commercially available PZT Quick-Pak patches, were bonded to Al beams that were progressively damaged. The damage was observed through changes in the electrical Impedance of the samples through the use of a Root Mean Squared Deviation damage metric, M. A corresponding change in M was observed in the Quick-Pak and ZnO embedded beams, however no significant change was observed in the beam bonded with the no ZnO composites.

6.2 Proposal of Future Work

Due to the promising results in structural health monitoring using ZnO nanowire embedded composites, possible future work would include bonding multiple ZnO

embedded composites to a structure and observing their ability to detect damage to different locations in the structure. Another future research opportunity would be to examine the piezoelectric properties of ZnO nanowire embedded in larger structures. Once validation of piezoelectric coupling was established, this property could be utilized to try detecting damage in the structure itself instead of a host structure. From there multiple leads could be attached to the structure in order to determine if different readings could be detected at different locations across the structure. Ultimately, diagnostic systems using computational models such as Artificial Neural Networks could be implemented to better detect locations and types of damage.

References

1. Lampe, M., M. Strassner, and E. Fleisch. *A Ubiquitous Computing environment for aircraft maintenance*. ACM.
2. Week, A., *World Military Aircraft Inventory*, in *Aviation week & space technology*. 2009, McGraw-Hill.
3. Jr., L.O.P. and B.C. Tonder, *External Strategic Analysis of the Aviation Maintenance, Repair and Overhaul (MRO) Industry and Potential Market Opportunities for Fleet Readiness Center Southwest*, in *Business*. 2009, Naval Postgraduate School.
4. A Pisupati, P., S.K. Dewangan, and R.K.G.V. V. *Enabling Technology for paradigm shift in next generation Aircraft Design and Maintenance*. 2011.
5. Balageas, D., C.-P. Fritzen, and A. Güemes, *Structural health monitoring*. Vol. 90. 2010: John Wiley & Sons.
6. Peairs, D.M., G. Park, and D.J. Inman, *Improving accessibility of the impedance-based structural health monitoring method.* Journal of Intelligent Material Systems and Structures, 2004. **15**(2): p. 129-139.
7. Khan, A., et al., *History current status and challenges to structural health monitoring system aviation field.* J. Space Technol., 2014. **4**(1): p. 67-74.
8. Inman, G.P.a.D.J., *Impedance-Based Structural Health Monitoring*, in *Damage Prognosis: For Aerospace, Civil and Mechanical Systems*, C.F.F. Daniel J. Inman, Vincente Lopes Jr., Valder Steffen Jr. , Editor. 2005, Wiley: West Sussex, England.
9. Su, Z., et al., *A built-in active sensor network for health monitoring of composite structures.* Smart Materials and Structures, 2006. **15**(6): p. 1939-1949.
10. Garcia, D., I. Trendafilova, and D.J. Inman, *A study on the vibration-based self-monitoring capabilities of nano-enriched composite laminated beams.* Smart Materials and Structures, 2016. **25**(4): p. 45011-45023.

11. Cattarius, J. and D.J. Inman, *TIME DOMAIN ANALYSIS FOR DAMAGE DETECTION IN SMART STRUCTURES.* Mechanical Systems and Signal Processing, 1997. **11**(3): p. 409-423.
12. Alibeigloo, A., *Static analysis of functionally graded carbon nanotube-reinforced composite plate embedded in piezoelectric layers by using theory of elasticity.* COMPOSITE STRUCTURES, 2013. **95**: p. 612-622.
13. Fan, Y. and H. Wang, *The effects of matrix cracks on the nonlinear bending and thermal postbuckling of shear deformable laminated beams containing carbon nanotube reinforced composite layers and piezoelectric fiber reinforced composite layers.* COMPOSITES PART B-ENGINEERING, 2016. **106**: p. 28-41.
14. Katzir, S., *The beginnings of piezoelectricity: a study in mundane physics*. Vol. 246. 2007: Springer Science & Business Media.
15. Ikeda, T., *Piezoelectricity*. 1990: Oxford university press.
16. Mason, W.P., *Piezoelectricity, its history and applications.* The Journal of the Acoustical Society of America, 1981. **70**(6): p. 1561-1566.
17. Heywang, W., K. Lubitz, and W. Wersing, *Piezoelectricity: evolution and future of a technology*. Vol. 114. 2008: Springer Science & Business Media.
18. Katzir, S., *The discovery of the piezoelectric effect.* Archive for history of exact sciences, 2003. **57**(1): p. 61-91.
19. Wang, Z.L., *Zinc oxide nanostructures: growth, properties and applications.* Journal of Physics: Condensed Matter, 2004. **16**(25): p. R829.
20. Wang, Z.L., *Nanostructures of zinc oxide.* Materials today, 2004. **7**(6): p. 26-33.
21. Pan, Z.W., Z.R. Dai, and Z.L. Wang, *Nanobelts of Semiconducting Oxides.* Science, 2001. **291**(5510): p. 1947-1949.
22. Yao, T. and S.-K. Hong, *Oxide and nitride semiconductors: processing, properties, and applications*. 1. Aufl. ed. Vol. 12. 2009, Berlin: Springer.
23. Wang, Z.L. and J. Song, *Piezoelectric nanogenerators based on zinc oxide nanowire arrays.* Science, 2006. **312**(5771): p. 242-246.
24. Masghouni, N., et al., *Investigating the energy harvesting capabilities of a hybrid ZnO nanowires/carbon fiber polymer composite beam.* Nanotechnology, 2015. **26**(9): p. 095401.

25. Takahashi, K., A. Yoshikawa, and A. Sandhu, *Wide bandgap semiconductors: fundamental properties and modern photonic and electronic devices*. 2007, New York;Berlin;: Springer.
26. *Wide Bandgap Semiconductors: Pursuing the Promise*, U.D.o. Energy, Editor. 2013: manufactoring.energy.gov.
27. Abdeljaber, O., et al., *Real-time vibration-based structural damage detection using one-dimensional convolutional neural networks.* Journal of Sound and Vibration, 2017. **388**: p. 154-170.
28. Zou, Y., L. Tong, and G.P. Steven, *Vibration-based model-dependent damage (delamination) identification and health monitoring for composite structures—a review.* Journal of Sound and vibration, 2000. **230**(2): p. 357-378.
29. Shull, P.J., *Nondestructive evaluation: theory, techniques, and applications*. Vol. 142.;142;. 2002, New York: M. Dekker.
30. Sohn, H., et al., *A review of structural health monitoring literature: 1996–2001*. Los Alamos National Laboratory, 2003.
31. Sun, F.P., et al., *Truss Structure Integrity Identification Using PZT Sensor-Actuator.* Journal of Intelligent Material Systems and Structures, 1995. **6**(1): p. 134-139.
32. Park, G. and D.J. Inman, *Impedance-based structural health monitoring.* Damage prognosis for aerospace, civil and mechanical systems, 2005: p. 275-292.
33. Farrar, C.R. and K. Worden, *An introduction to structural health monitoring.* Philosophical Transactions of the Royal Society of London A: Mathematical, Physical and Engineering Sciences, 2007. **365**(1851): p. 303-315.
34. Rajan, G. and B.G. Prusty, *Structural health monitoring of composite structures using fiber optic methods*. Vol. 60. 2016, Boca Raton: Taylor & Francis, a CRC title, part of the Taylor & Francis imprint, a member of the Taylor & Francis Group, the academic division of T&F Informa, plc.
35. Woike, M., M. Clem, and A. Abdul-Aziz. *Structural Health Monitoring on Turbine Engines Using Microwave Blade Tip Clearance Sensors*.
36. Mitra, M. and S. Gopalakrishnan, *Guided wave based structural health monitoring: A review.* Smart Materials and Structures, 2016. **25**(5): p. 53001-53027.

37. Raghavan, A. and C.E. Cesnik, *Review of guided-wave structural health monitoring.* Shock and Vibration Digest, 2007. **39**(2): p. 91-116.
38. Lopes, V., et al., *Impedance-Based Structural Health Monitoring with Artificial Neural Networks.* Journal of Intelligent Material Systems and Structures, 2000. **11**(3): p. 206-214.
39. de Oliveira, M.A. and D.J. Inman, *Performance analysis of simplified Fuzzy ARTMAP and Probabilistic Neural Networks for identifying structural damage growth.* Applied Soft Computing, 2017. **52**: p. 53-63.
40. Cartwright, H.M., *Artificial neural networks*. Second;2nd 2015; ed. Vol. 1260.;1260;. 2015, New York: Humana Press.
41. Livingstone, D., *Artificial neural networks: methods and applications*. Vol. 458;458.;. 2008, Totowa, NJ: Humana Press.
42. Shanmuganathan, S., S. Samarasinghe, and SpringerLink, *Artificial Neural Network Modelling*. 1st 2016. ed. Vol. 628. 2016, Cham: Springer International Publishing.
43. Kamruzzaman, J., R. Begg, and R.A. Sarker, *Artificial neural networks in finance and manufacturing*. 2006, Hershey, PA: Idea Group Pub.
44. Meitzler, A., et al., *IEEE standard on piezoelectricity*. 1988, Society.
45. Tsai, M. and K. Wang, *On the structural damping characteristics of active piezoelectric actuators with passive shunt.* Journal of Sound and Vibration, 1999. **221**(1): p. 1-22.
46. Meirovitch, L., *Fundamentals of vibrations*. 2001, Boston: McGraw-Hill.
47. Beards, C.F., *Structural vibration: analysis and damping*. 1 ed. 1996, New York;London;: Arnold.
48. Yang, Y., et al., *Size Dependence of Dielectric Constant in a Single Pencil-Like ZnO Nanowire.* NANO LETTERS, 2012. **12**(4): p. 1919-1922.
49. Chen, C.Q., et al., *Size dependence of Young's modulus in ZnO nanowires.* PHYSICAL REVIEW LETTERS, 2006. **96**(7): p. 075505.
50. Liang, C., F.P. Sun, and C.A. Rogers, *Coupled Electro-Mechanical Analysis of Adaptive Material Systems — Determination of the Actuator Power Consumption*

and System Energy Transfer. Journal of Intelligent Material Systems and Structures, 1994. **5**(1): p. 12-20.

51. Liang, C., F. Sun, and C. Rogers, *Coupled electro-mechanical analysis of adaptive material systems-determination of the actuator power consumption and system energy transfer.* Journal of intelligent material systems and structures, 1997. **8**(4): p. 335-343.
52. Giurgiutiu, V. and C.A. Rogers, *Modeling of the electro-mechanical (E/M) impedance response of a damaged composite beam.* Adaptive Struct. Mater. Syst, 1999. **87**: p. 39-46.
53. Offenberger S., B.A., Emami A., Al-Haik M., and Philen M. K., , *FIBER REINFORCED COMPOSITES WITH ZINC OXIDE PIEZOELECTRIC NANOWIRES FOR STRUCTURAL HEALTH MONITORING AND ENHANCED INTERLAMINAR STRENGTH*, in *20th International Confernece on Composite Materials*. 2015: Copenhagen, Denmark.